RSC Advances

ROYAL SOCIETY OF CHEMISTRY

www.rsc.org/advances

Liquid phase collagen modified graphene that induces apoptosis

***Soumya Bhattacharya*[1], *Swati Mishra*[1], *Pallawi Gupta*[2], *Pranav*[2], *Mainak Ghosh*[1], *Ashit Kumar Pramanick*[1], *Durga Prasad Mishra*[3] *and Suprabha Nayar*[1*]**

[1] Materials Science and Technology Division, CSIR-National Metallurgical Laboratory, Burmamines, Jamshedpur-831 007, India

[2] Centre for Nanotechnology, School of Engineering and Technology, Central University of Jharkhand, Ranchi – 835 205, India

[3] Cell Death Research Laboratory, Endocrinology Division, CSIR-Central Drug Research Institute, Lucknow-226 031 India

[*]Tel.: +91-(657) 2345077, Fax: +91- (0657) 2345213, E-mail:suprabha.nayar@gmail.com

ABSTRACT

Direct exfoliation of graphite (GR) to collagen modified graphene (G) flakes using acylated collagen has been studied. The chemical structure of collagen (CL) and all liquid exfoliants studied so far have a striking similarity, namely, hydrocarbon chain length, aromatic residues and polarity. Here, CL dispersed in acetic (AA), succinic (SA) and propionic (PA) acid behaves as three different surfactants which have been used to simultaneously exfoliate and disperse nano G platelets to a colloidal form. Transmission electron microscopy micrographs show average dimensions of ~ 500 × 200 nm; Moiré patterns observed at several places in all the three samples indicate periodic perturbations in the graphitic stacking and selected area electron diffraction confirms graphene formation. AFM images confirmed the same lateral dimensions with an average thickness of 1.2 nm. The Raman spectra revealed strain dependent splitting and red shift of 2D bands, maximum in G-PA and minimum in G-AA. X-ray photoelectron spectroscopy showed a decrease of the sp^2/sp^3 ratio GR post CL interaction indicating interaction. The zeta potential, fluorescence and luminescence values changed in G, with maximum variation in G-PA; suggesting that CL dispersed in PA as the best. The bioactivity of colloidal G-PA was studied in solid, hematological and neuronal cancer cell lines. It induced reactive oxygen species and cell death in cancer cell lines and altered membrane integrity while sparing normal cells, underscoring its possible utility in cancer therapy.

Keywords: colloidal graphene, collagen, surfactants, apoptosis

1. INTRODUCTION

Increasing applications of graphene (G) are demanding its bulk production which is possible relatively easily by liquid phase exfoliation of graphite (GR). The main benefits of liquid exfoliation are i) ease of production ii) safety and iii) non-volatility. The common procedure of G formation is oxidation of GR to graphite-oxide (GO) using oxidizing agents followed by reduction to G/ reduced graphene-oxide (rGO), the oxygen moieties often difficult to remove [1,2]. The emphasis these days is on the direct exfoliation of G that is free of basal-plane defects separated and stabilized in a colloidal form. Extensive work on the liquid phase exfoliation method has shown that GR in organic polar solvents (N-methyl-2-pyrollidone (NMP), Dimethylacetamide (DMA), gamma-Butyrolactone (GBL) and 1, 3 Dimethyl-2-imidazolidinone (DMEU)) yields a mixture of single-layer (SLG) and few-layer (FLG) G platelets[3]. Exfoliation using sodium dodecylbenzene sulfonate (SDBS) and ionic liquids like 1-butyl-3-methyl-imidazolium bis (trifluoromethanesulfonyl) imide has also been attempted[4,5]. The direct method of exfoliation is gradually picking up momentum because of its obvious advantages of low defects and oxygen content, i.e., it avoids the compositional and structural defects induced by the conventional methods. In this study, we have used acylated CL as surfactants[6], to simultaneously exfoliate and stably disperse GR into collagen modified graphene flakes at ambient conditions. The dispersibility of graphene is proportional to the magnitude of the electrostatic potential and steric potential barriers for different surfactants[7]. CL with every third amino acid as glycine and a predominance of aromatic hydroxyproline provides the required shear for exfoliation. This allows immense scope of charge transfer between the carbon layers of graphite and the CL protein, which can be seen as a series of electron-rich and electron deficient media for exfoliation that perturbs the Van der Waals forces between the graphitic layers. Such charge transfer

between the electron-rich graphitic layers and electron-deficient aromatic CL moieties seem to be the driving force for the interaction of GR and CL. The periodic gaps of CL provide a site for covalent binding and unwound helices at the two ends of 0.5nm, kind of forces its way into the graphitic stacks and enables exfoliation[8]. CL was dispersed in three different organic acids namely acetic acid (AA), propionic acid (PA) and succinic acid (SA); these were used to incubate GR at room temperature and the samples named G-AA, G-PA and G-SA respectively. The rupture of interstrand H-bonds post acylation in CL exhibits particularly large rupture forces, multitude of which affects the stability of the CL differently in the three acids (Figure 1). Reports suggest that covalent functionalization at the graphitic edges with bulky groups induces strain that result in exfoliation. When such a bulky group is a protein, major dislocation of the electron cloud occurs which allows CL helices to force its way through the graphitic stacks and exfoliate them. It is a known fact that lowering the surface tension between water and the surface of GR facilitates exfoliation; the exfoliation is brought about by surfactants which match the surface energy of individual graphitic stacks, the surface energy of AA, PA and SA are not close to that of graphite[3,9] , but with CL they act as surfactants [6]. Very few research groups have attempted the exfoliation of GR using proteins; previous work using genetically engineered protein, HFBI, is a major step in this direction but genetic engineering of proteins is tedious and cost intensive [10-11]. More recently, a simple green route for reduction of GO to G has been reported using non-aromatic and thiol-free amino acids[12]. The highlight of our process is the ambient conditions and the mild sonication, which reduces sonication induced scissions. We face problems in calculating the yield as the ultraviolet (UV) absorbing regions of graphene and protein overlap. We have not yet made an attempt to remove CL as our targeted applications have been predominantly biomedical and CL helps binding of other biomolecules. Cancer cell studies show that G-PA

nanoflakes in a colloidal form induce cytotoxicity in cancer cells while sparing the primary non cancerous cells. In addition, our latest publication on electrical transport property proves that collagen modified graphene is very close to that of pristine graphene[13].

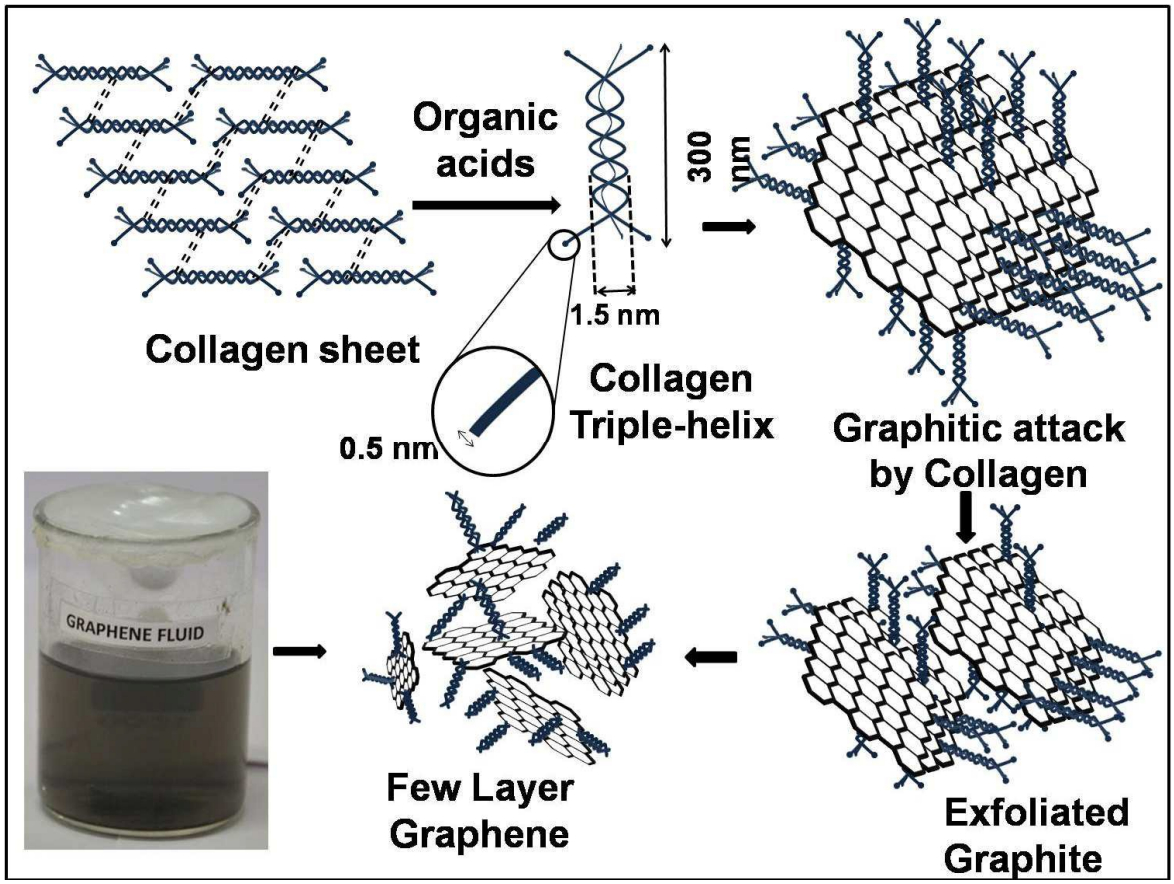

Figure1. A common schematic representation of GR exfoliation by acylated CL for all three acids

2. EXPERIMENTAL PROCEDURE

2.1 Synthesis. High purity natural GR powder (~ 200 meshes ~75µm) from Alfa Aesar and CL Type I from bovine Achilles tendon was from Sigma-Aldrich. Glacial AA, PA and SA were from Merck. Two percent (w/v) stock CL dispersions were prepared i with constant stirring and

mild heating at 40^{o}C; the stirring was continued for 24 hrs followed by centrifugation. The CL dispersions diluted to 0.01 % (w/v) and GR powder added to maintain a constant GR: CL ratio of 1:1. The dispersions were incubated for 7 days after which they were subjected to mild sonication (150 Watts, 40 KHz) for 10 mins at regular intervals of 5 mins, thrice. It was followed by centrifugation at 8000rpm for 30 mins; the supernatant used for all characterization.

2.2 Characterization. Transmission electron microscopy (TEM) was done in analytical Philips CM200 microscope at 200kV; all dispersions were dried on carbon coated copper grids (~ 300 meshes) and then imaged. The hydrodynamic diameter (D_H), polydispersity index (PdI) and zeta potential was measured by dynamic light scattering (DLS) NANO 100 zetasizer. Atomic force microscopy (AFM) was done in Bruker VEECO microscope in the non contact mode at ambient conditions using pyrex glass cantilever with silicon tip; the scanning speed was 0.5 Hz. A drop of the dispersion was dried on glass substrate and the surface imaged; post processing and image analysis was done using the NanoScope Analysis software. Surface enhanced Raman spectroscopy (SERS) spectra was recorded in Nicolet, Almega^{XR} dispersive Raman spectrometer (using a Nd: YAG laser source, λ = 532 nm) by drying a drop of the samples on polished copper substrates for surface enhanced signals. X-ray photoelectron spectroscopy (XPS) spectra were recorded using a Specs spectrometer with MgK_{α} source (1253.6 eV). Few drops of the dispersions were dried on glass substrates and then inserted into a vacuum chamber having a pressure ~ 10^{-9} Torr. Spectra were de-convoluted using CASA XPS software, post Shirley background subtraction. All the peaks were calibrated with respect to the standard C1s binding energy peak of pure GR at 284.5eV. Photoluminescence (PL) and fluorescence (FL) were measured using a Hitachi F-4500 spectrophotometer at an excitation wavelength of 280 nm and emission scan range from 290 - 900 nm for PL and 290 – 450 nm for FL.

2.3 Cell Culture. All the cell lines were obtained from the American Type Culture Collection (ATCC; Manassas, VA, USA). The sources of the normal cells described previously [12-13]. Briefly the cells were cultured in Roswell Park Memorial Institute (RPMI) 1640 medium supplemented with 10% heat inactivated fetal calf serum, 10 mmol/L glutamine, and 50 μg/mL each of streptomycin and penicillin[14]. The G suspension was diluted to appropriate concentrations from 20 - 100 μg/mL with the culture medium prior to treatment. Cells were grown to 60% confluence before interaction with G for 24h in a humidified incubator at 37°C with 5% CO_2. Cells not treated with G served as controls.

2.4 ROS Quantification. The quantification of the intracellular ROS was done using the fluorescent dye 2′7′-dichlorodi-hydrofluorescein diacetate (Invitrogen, Carlsbad, CA, USA) according to a previously standardized protocol[15].

2.5 Membrane Integrity Assay. The cell membrane integrity of was evaluated by determining the activity of lactate dehydrogenase (LDH) released from the cells using an in vitro assay based on the release of the cytosolic enzyme, from cells with damaged cellular membranes toxicology assay kit (TOX7, Sigma-Aldrich) [15]. Briefly, cells were exposed to various concentrations of G for 24 hours then 100 μL per well of each cell-free supernatant was transferred in triplicate into wells in a 96-well plate, and 100 μL of LDH-assay reaction mixture was added to each well. After 3 hours incubation under standard conditions, the optical density of the color generated was determined at a wavelength of 490 nm using a BMG fluostar omega spectrofluorimetry.

2.6 Cell Death Assay. Cell death post G treatment was measured by using the 7AAD/ Annexin V Apoptosis detection kit (Invitrogen, Carlsbad, CA, USA) according to the manufacturer's

instructions[14]. The samples were analyzed for live, necrotic, early and late apoptotic cells using FACS Caliber (BD Bioscience, San Jose, California, USA) flow cytometer.

2.7 Statistical Analysis. All data were expressed as mean ± S.D. Statistical analysis of the data using the Graphpad Prism 5.0 software (GraphPad Prism Software Inc., San Diego, California, USA). All comparisons between the treatment groups done using two-tailed paired student's t-test. Differences were considered significant at a 0.05 level of confidence.

3. RESULTS AND DISCUSSION

Usage of CL as a direct exfoliant is based on our experience of biomimetic synthesis and the existence of a patent[6] claiming CL as a surfactant with organic acids.

3.1 Transmission Electron Microscopy. G is a two-dimensional sheet consisting of hexagonal carbon lattice with delocalized π electrons. Studies on the molecular packing of type I CL has revealed quasi hexagonal packing of CL fibrils in the lateral plane with a triclinic unit cell, unit cell parameters are: a = 39.97Å, b = 26.95Å, c = 677.9 Å, $\alpha = 89.24^{o}$, $\beta = 94.59^{o}$ and $\gamma = 105.58^{o}$ [16-18]. The lattice constants of which are much bigger than GR (space group: $P6_3/mmc$, a= 2.47 Å and c = 6.80 Å) and are not detected in the analytical TEM operating at 200kV; the focal length being too low to measure diffraction from the CL lattice. TEM images of CL modified G platelets in the three organic acids show average dimensions of ~500 × 200 nm and qualitative electron dispersive spectroscopy (EDS) spectrum endorsed the presence of nitrogen corroborating the co-existence of protein and G (data not shown).

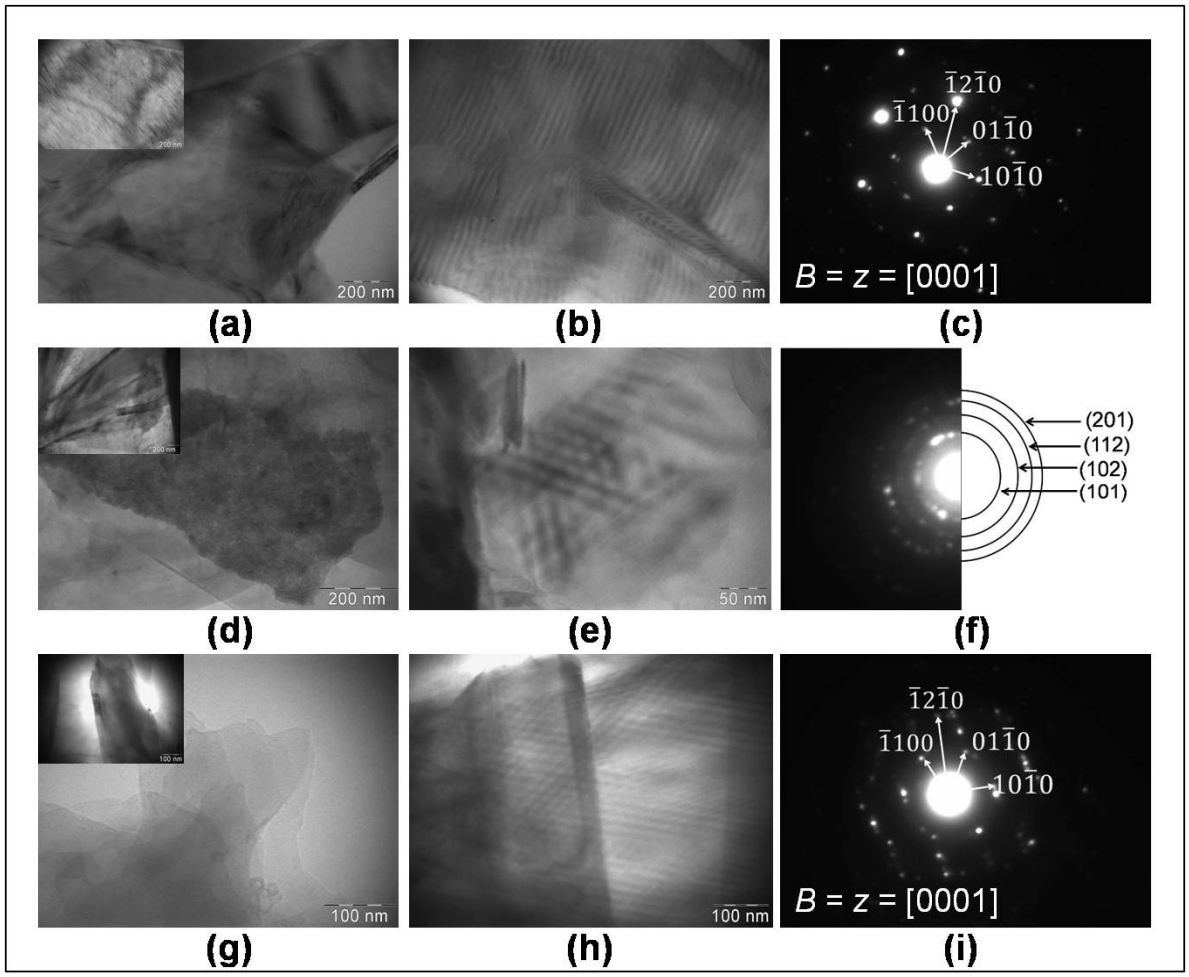

Figure2. TEM micrographs with indexed SAD patterns of (a-c) G-AA, (d-f) G-SA and (g-i) G-PA; the zone axis [z]=[0001] is mentioned for (c) and (i)

TEM micrographs reveal that exfoliation and functionalization into colloidal G platelets occurs simultaneously; at first acylated CL attacks parent graphitic stacks, because of the shear forces, CL molecules slowly penetrate the layers and rip apart few layer thick G platelets. The only difference in the three acids is in the site and rate of acylation of CL, which affects G exfoliation and stabilization. The hydroxyproline sites of CL get acylated in AA and PA while hydroxylysine sites get acylated in SA, the acylation in AA and PA are also different because of the additional -CH_2 group in PA. G-AA in Figure 2a exhibits typical flaky sheet like morphology

with thick edges, this remained invariant in all the areas of this sample. Figure 2a (inset) clearly shows numerous striations signifying crystallographic defects that have been introduced into the GR layers at regular intervals. Clearly pronounced parallel Moiré patterns with only minor variation in spacing is rampant in this sample, shown in Figure 2b. This particular observation confirms periodic attack by CL; fringes oriented differently can occur from any direction and that causes a disturbance in the arrangement of the layers. In other words, the interlayer atomic alignment of GR gets disturbed and induces strain; there is an angular misorientation between consecutive sheets. The indexed selected area diffraction (SAD) pattern (Figure 2c taken from 2a) confirms hexagonal symmetry. It was observed that the intensity of the diffraction spots from $\{11\bar{2}0\}$ family of planes corresponding to the 2nd order Laue zone was greater than the first order reflections from $\{10\bar{1}0\}$ planes, the zone axis was along [0001] direction. Such an observation has been previously reported for FLGs[4,10]. Under the diffraction conditions used, angular difference between the radius vector R1 $\{10\bar{1}0\}$ and R2 $\{01\bar{1}0\}$ was 58^0, whereas between R2 $\{01\bar{1}0\}$ and R3 $\{\bar{1}100\}$ it was 62^0. Deviation from perfect hexagonal symmetry ($\theta=60^0$) indicates lattice distortion due to exfoliation.

G-SA showed polycrystalline spongy (Figure 2d) collagen modified G platelets with the presence of folds, crinkles and rolled edges (inset Figure 2d). The possible reason for the folds (not seen in G-AA sample) was the decrease in sheet thickness, because of which it is unable to maintain a planar nature. The reduction of sheet thickness in turn could be due to enhanced acylation of CL in SA by the dicarboxylic groups at the hydroxylysine site which though is able to effectively bind to GR is unable to rip apart GR flakes. Even though the number of hydroxyproline residues is more than the hydroxylysine residues in type 1 CL, the proximity of

the dicarboxylic groups seems to have a more devastating effect as a surfactant[19]. Within a reduced stack also, the layer orientation was different (Figure 2d, inset). As discussed before, the attack at the GR edges by bulky aromatic groups of the protein leads to stress which rotate consecutive graphitic layers disturbing the Bernal stacking. When the electron beam is incident on such a disordered structure, constructive interference occurs due to diffraction from self-assembled layers within the disordered regions resulting in criss-cross checker board like appearance of the Moiré pattern (shown in Figure 2e); the angular mismatch between the layers was equal to 55^0. Here, Moiré fringe is not a global phenomenon envisaging local heterogeneity in microstructure in terms of thickness and sheet orientation. Contrary to the spot patterns observed in case of G-AA and G-PA, SAD pattern (Figure 2f) taken from the region in Figure 2d showed polycrystalline rings indicating reduction in the crystallite size of G-SA compared to the others.

G-PA was characterized by thin nearly transparent irregular shaped few layer G nanoplatelets with clearly defined straight boundary, transparency being a characteristic of very thin G layers, best seen in (Figure 2g inset) with four well defined edges. Similar to G-SA, the checker board like structure was also seen here in the well developed Moiré pattern (Figure 2h); the only difference was the angle which increased to 127^0. The SAD (Figure 2i) confirmed the hexagonal symmetry with brighter 2^{nd} order Laue zone similar to G-AA. Presence of dual spots adjacent to one another corresponding to the $\{10\bar{1}0\}$ planes signify electron diffraction from two misoriented G layers, one on top of another with small angular deviation of 8^0 between them. The presence of the additional $-CH_2$ group changes the hydrophobic hydration layer (described in the next section) which causes the many defects seen in G-AA to break up in G-PA.

To ascertain any change in the interplanar spacing of graphite post exfoliation, powder diffraction of dried dispersions were done. As expected, it was observed that compared to precursor GR (d_{hkl} = 3.351 Å), the d_{hkl} spacing of G-AA (3.351Å) was unchanged, however the spacing was slightly reduced in G-SA (3.350 Å) and G-PA (3.339Å); A change in d spacing is expected only if CL has intercalated within the layers and remains there; in our case, the stacks have broken down into 200-500 nm graphene nanoplatelets as established from all other characterizations but individual sheets have not been ripped apart.

3.2 Atomic Force Microscopy. Atomic force microscopy of the CL protein (served as control) and all the three samples G-AA, G-PA and G-SA were done and the edge thickness and lateral dimensions of the graphene sheets inferred from 1 × 1μm area images (the initial scanning was done in 10 × 10μm). The helical nature of the collagen was visible in the phase microscopy images of CL (not shown), however, no stiffness change was noted during AFM scanning. The micrograph had uniform contrast; however, after magnification the overlapping gap regions (60-70 nm) of the CL triple helix were visible. Due to the presence of graphene in all the samples a distinct change in the stiffness was observed during scanning which appeared as valleys indicating different phase regions. Almost transparent sheets were visible in the regions where the helical nature was disturbed indicating graphene formation. The lateral dimensions of the platelets were on an average within 200-500 nm (shown in Figure 3); in G-AA, the thickness is equal to 1.3 nm corresponding to 4 layers; in G-SA the thickness increased to 1.6 nm signifying 5 layers followed by G-PA which had a thickness of 1nm equal to 3 layers in the recorded images. It must be mentioned that the in our experiments very mild sonication (150 Watts, 40 KHz for 10 mins at regular intervals of 5 mins) in a bath was done, sonication at higher wattages would results in further uniformity in all three samples.

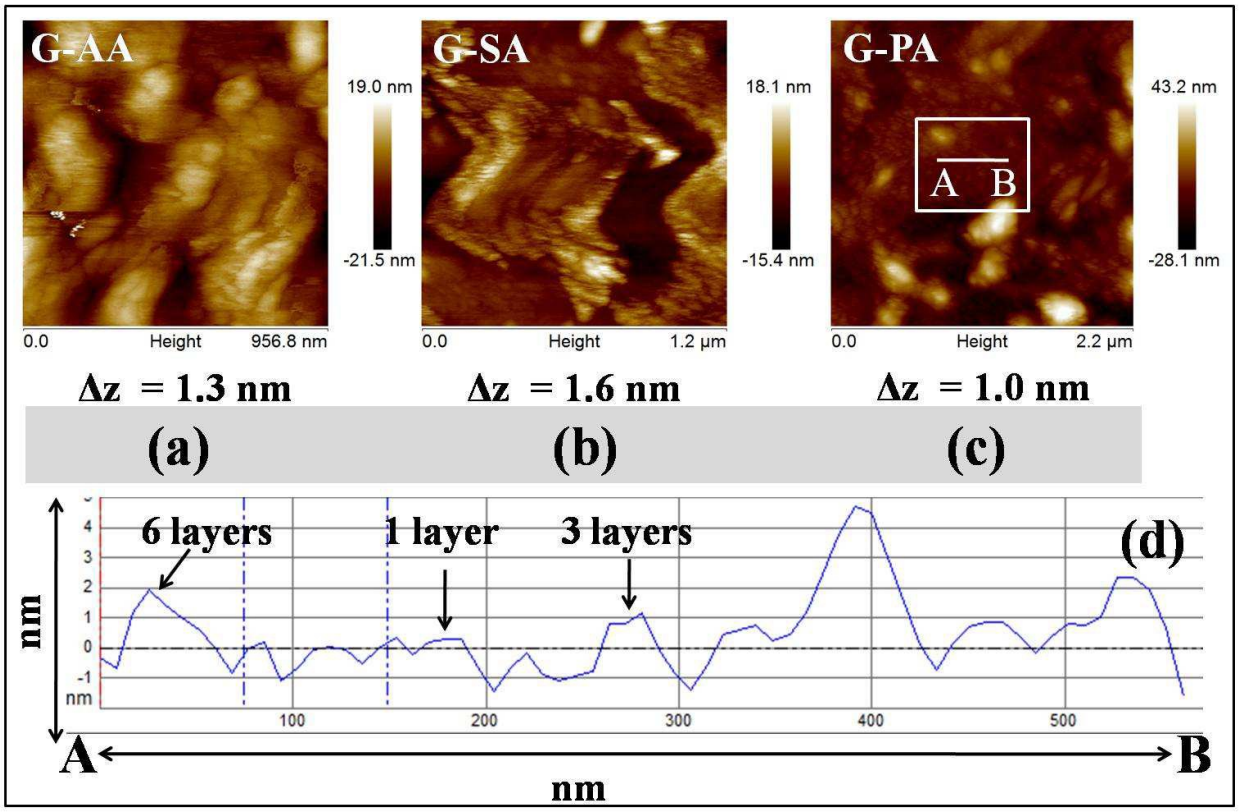

Figure3. AFM images showing the formation of collagen modified graphene nanoplatelets taken in the non contact mode; ΔZ signifies the difference in the height profile of (a) G-AA, (b) G-SA and (c) G-PA; (d) sectional analysis of the height along the length AB in the G-PA sample, the selected region is 550nm wide

3.3 Dynamic Light Scattering. Table 1 shows the values for CL dispersions with and without FLGs, well within the colloidal range. This process seems to be both charge and steric stabilized. The diameter of the CL molecules is highest in CL-AA followed by CL-SA and CL-PA; this shows that CL-AA has a marginally more open structure compared to the other two; PA is able to keep the CL helical strands about 50nm closer compared to AA.

Samples	Zeta Potential	Hydrodynamic	Polydispersity

	(ξ, mV)	Diameter (D_H, nm)	Index (PdI)
CL-AA	+ 36.0	507.0	0.296
G-AA	-26.0	256.2	0.400
CL-SA	+ 36.2	487.5	0.362
G-SA	-15.9	275.0	0.453
CL-PA	+ 31.5	452.6	0.311
G-PA	+ 26.7	295.5	0.496

Table 1. Hydrodynamic diameter (D_H), zeta potential (**ξ**) and polydispersity index (PdI) of the G dispersions

However, when GR is added, the structure contracts, a fact observed for all the samples; as the hydrophilic-hydrophobic interaction dominates, it closes the structure, proportionate to the hydrophobic hydration capability. Hydrophobic hydration behaves oppositely to polar hydration, as their associated disorganized hydrogen bonds is already bent or broken. In addition, it is accompanied by multiple van der Waals interactions between water and the hydrophobic material. Introduction of the $–CH_2$ groups in PA thus reverses the sequence of size variation with the maximum size recorded for G-PA[20]. The variation of the D_H can be explained based on the facts that the CL: GR ratio is not optimized, and that the PdI is also the highest for G-PA. In addition, due to the high surface area and surface activity, the 500nm FLG platelets would tend to aggregate if not stabilized by surfactants[21]. As a test for stability, these fluids were subjected to centrifugation, CL at 8000rpm tends to settle and therefore, there is a difference in the FLG content and hence the coloration of the fluid, pre and post centrifugation. After functionalization,

the G surface acquires characteristics of the functionalizing agent and the surface potential changes in accordance with the pH of the dispersion (G-AA=7.3, G-SA= 7.2 and G-PA 3.9); hence the difference in the zeta potential (Table 1). It is reported that ionic surfactants stabilize graphene sheets with a concentration tat increases with the square of the Zeta Potential[22].

3.4 Raman Spectroscopy. Raman spectra were measured using the 532nm line of Argon laser as excitation source at room temperature. A change of the polarization potential/deformation of the electron cloud is necessary for a molecule to exhibit Raman Effect, an effective tool to confirm the difference in the interaction of CL and GR. The three most intense Raman features are at ~ 1580 cm^{-1} (G band), ~ 1350 cm^{-1} (D-band) and ~ 2700 cm^{-1} (2D band); in addition to these, a band at ~1620 (D′band) may or may not be present. The G band is an in-plane vibrational mode involving the sp^2 hybridized carbon atoms in carbon nanostructures; the D and D′ bands are defect induced features. The intensity of the D peak is attributed to the disorder but not related to the number of layers and normally the peak intensity ratio I_D/I_G is measured to ascertain the degree of disorder. From Figure 4a we can see that there is not much of a difference in the G peak positions of G-AA, G-SA and G-PA. Notably, the D band is only visible in G-AA; in addition, it is also reported that with increasing sp^3 content the D signal weakens; SA and PA

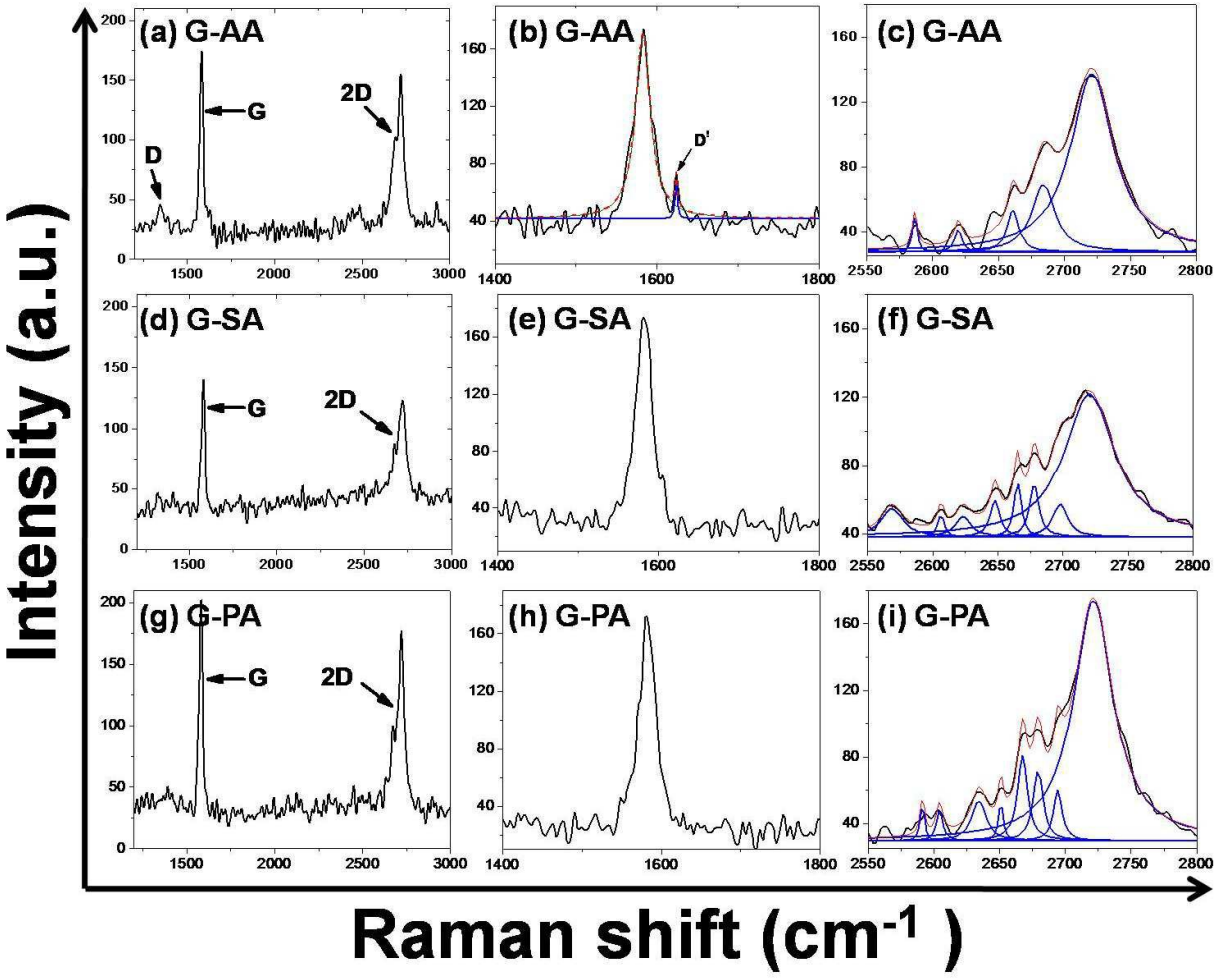

Figure 4. Raman spectra showing the full spectra, G and 2D bands of (a-c) G-AA, (d-f) G-SA and (g-i) G-PA

being better surfactants, this fact was confirmed from subsequent XPS measurements which showed more interaction of GR with SA and PA (Table 2)[23]. In addition to the D band, the D′ band was detected only in case of G-AA signifying crystallographic defects like dislocations/stacking faults which correlates well with the TEM (Figure 4a inset & b) and AFM data. The 2D band however, is not defect induced and represents the stacking order; interestingly, the highly broadened 2D bands of both G-SA and G-PA (shown in Figure 4f and i)

were fitted with Lorentzian line shape function using Origin 8.0 software and deconvoluted into 7 components within the range 2600-2800 cm^{-1}; the major component was positioned at 2720 cm^{-1} with minor peaks at 2694, 2678, 2667, 2651 and 2633 cm^{-1}, progressively red shifting to lower wave numbers; on the other hand, the 2D band of G-AA (Figure 4c) consisted of only 4 components (2720, 2684, 2661 and 2619 cm^{-1}). The change in Raman band width (estimated from FWHM in eV) and shape may be due to the loss of Bernal stacking of the GR layers as a result of interaction of CL molecules[24-25]. This loss in stacking results in the formation of arrays of partial dislocations and stacking faults on the basal planes; twisting and rotation of the layers is clearly visible from the Moiré fringes in the TEM micrographs (Figure 2e & h). It is to be noted that the red shift of the 2D band is dependent on the stress exerted on the layers; acylated CL brings down the surface energy between GR and water, the molecules adhere and bond with the carbon atoms exerting pressure as they interact with GR flakes resulting in lattice distortion. Previous work on G composites have revealed that the band shift to lower wave numbers and broadening of the spectrum increases as the strain increases due to electronic charge transfer between the aromatic ring of hydroxyproline and hydroxylysine amino acids of CL and the carbon atoms of GR[24].

3.5 X-ray photoelectron spectroscopy. XPS showed interaction of the CL molecules with the sp^2 hybridized carbon atoms of GR, extremely sensitive to the chemical environment that causes a shift in the binding energy. The shift depends on the nature of the chemical ligands that bind with the carbon atom; electron donating groups (e.g. NH_2, OH^-, O^{2-}) increase the binding energy and electron acceptor groups decrease it. The full spectra (not shown) of the samples was taken in the range 0-1100eV; they consist of C1s (~284.5 eV), O1s (~534eV) and N1s (~401eV) core level peaks; the N1s was for protein signature from CL, which was not present in GR. To

calculate the percentage of functional groups, peak shift and broadening, the C1s peaks were de convoluted using CASA XPS software considering Voigt functions; the Gaussian and Lorentzian line shapes were adjusted in each case with 30% Gaussian and 80% Lorentzian character for GR; the remaining were fitted with 30% Gaussian and 70 Lorentzian character; all fitting were done post Shirley background subtraction. The C1s spectrum of GR consisting mainly of sp^2 carbon had a broad asymmetric tail towards the higher binding energy as shown in Figure 4a. It showed a highly intense and sharp peak at 284.5 eV corresponding to sp^2 hybridized C-C/C=C bonds in the hexagonal lattice along with a minor component at 285.56 eV corresponding to sp^3 C-OH bonds due to surface adsorption of water molecules[26]. The shake-up peak at 289.43 eV correspond to the π-π^* transition in GR. The ratio of the sp^2 and sp^3 domains was ~ 4.59 indicating highly pure GR. After interaction, the sp^3 character becomes more pronounced; reflected in the C1s peak which becomes more symmetric with enhanced broadening towards higher binding energy (Figure 5(b-d)). It is difficult to uniquely peak fit such mixed sp^2/sp^3 spectra; however, peaks corresponding to C-NH (amine, ~288eV), C=O (carbonyl, ~288.1 eV), C-O (~285.5eV) and C-OH (hydroxyl, ~ 285.5eV) groups could be easily detected (spectral parameters shown in Table 2) [27]. The sp^2/sp^3 ratio in G-AA, G-SA and G-PA progressively decreased from 2.08 to 1.61 to 1.46 which proves that CL dispersed in PA is the most efficient. The broadening determined from FWHM is practically same in all three G-AA (2.12eV), G-PA (1.99eV) and G-SA (2.07eV), however the concentration of the peak at ~288 eV progressively increases from 9.60% (G-AA) to 10.92% (G-SA) to 16.68% (G-PA); highest in G-PA proving that the CL-PA interacts the most with GR layers.

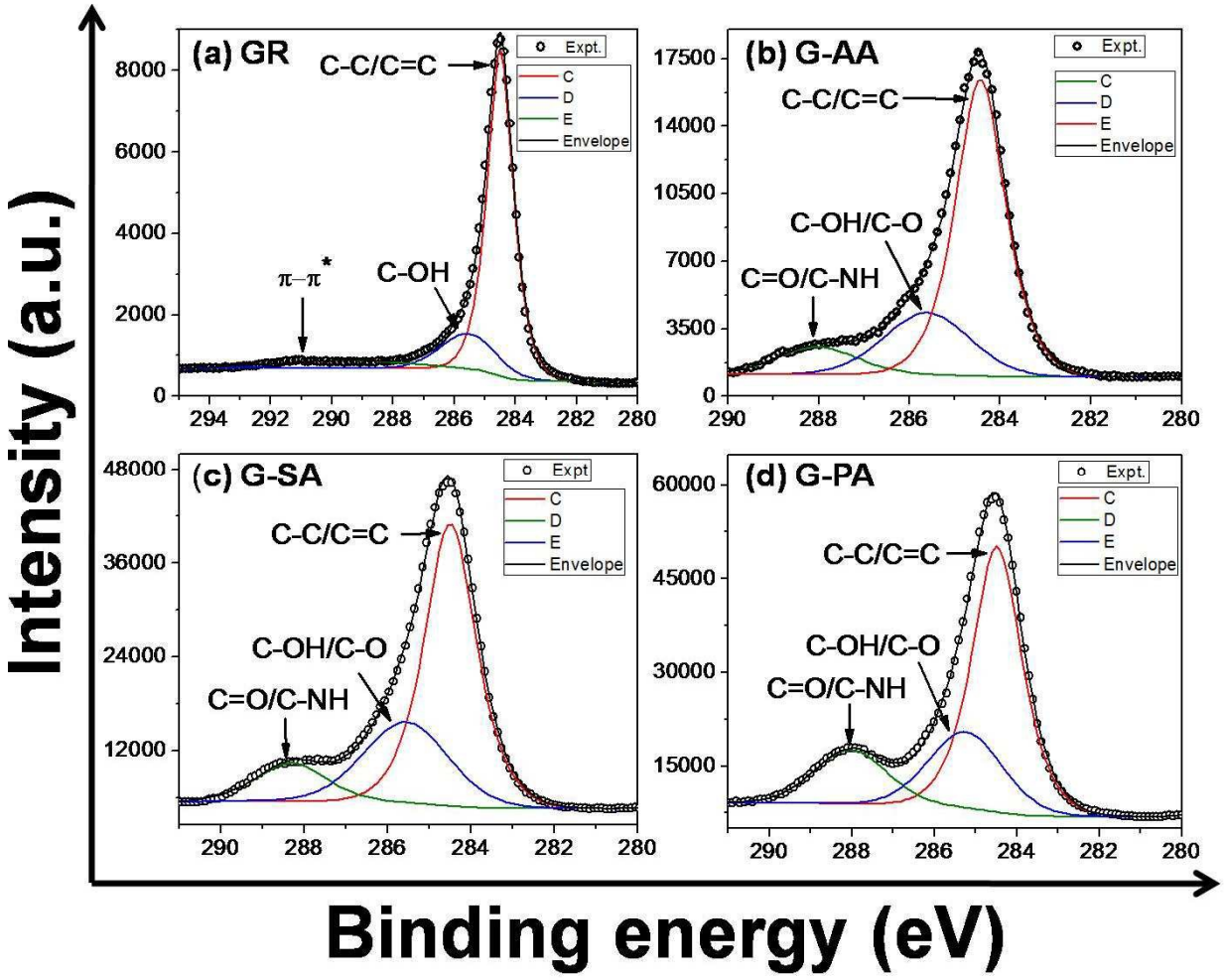

Figure 5. XPS spectra of (a) GR, (b) G-AA, (c) G-SA and (d) G-PA dispersions. The increase in peak width and shift towards higher binding energy signify interaction of CL with GR

Sample	Binding Energy (eV)	Bond assignment	FWHM (eV)	Relative % conc.	sp^2 / sp^3
	284.50	C-C/C=C	0.98	75.50	
GR	285.56	C-OH	2.12	16.43	4.59
	289.43	π-π^*	5.01	8.02	
	284.43	C-C/C=C	1.29	67.54	
G-AA	285.61	C-OH/C-O	2.22	22.86	2.08
	288.03	C=O/C-NH	2.12	9.60	
	284.49	C-C/C=C	1.46	61.75	
G-SA	285.55	C-OH/C-O	2.40	27.33	1.61
	288.30	C=O/C-NH	1.99	10.92	
	284.47	C-C/C=C	1.42	59.46	
G-PA	285.23	C-OH/C-O	2.12	23.86	1.46
	288.02	C=O/C-NH	2.07	16.68	

Table2. Parameters showing binding energy (eV), chemical bonds, full width at half maximum (FWHM, eV), relative % concentration and sp^2/sp^3 ratio of spectral components of the deconvoluted C1s peaks

3.6 Fluorescence and Luminescence. It must be mentioned that for CL in organic acids, there are interferences in the UV absorption; FL spectrophotometer is more sensitive. The FL spectra (Figure 6) were recorded for all samples including CL-organic acid dispersions, it was observed that prior to GR interaction, CL-SA showed the highest and most broadened FL peak, indicating the most conformational change expected because of the dicarboxylic acid. After GR interaction, severe quenching of FL was observed in case of CL-SA; as pure G does not fluoresce, this occurred due to interaction with CL. Interestingly, G-PA and G-SA showed almost similar FL. Recently, it has been reported that the quenching effect originates from the FL resonance energy transfer, or non-radiative dipole-dipole coupling between the FL species for e.g., amino acid residues and GR layers during exfoliation[28]. Due to the charge transfer between these surfactant molecules and the GR edges, a band gap is created and localized recombination of electron-hole pairs in the sp^2 domains has been suggested as the origin of FL[29]. Previous work has revealed that FL can originate from the electronic transition at the interface between the defect free carbon regions and defective sites at the GR edges and/or the basal planes; bond distortion due to stacking disorder akin to our system, may also contribute to FL. Because G has no band gap, no PL (shown in Figure 7) is expected upon the relaxation of charge carriers; however, in chemically modified G, the weak inelastic scattering results in PL as electronic cloud is affected. Nitrogen functionalization of G increases the intensity of PL and shifts it to shorter wavelength; in our case though there is no change in the peak position centered on 558nm the intensity of G-PA is the highest followed by G-SA and G-AA. Enhanced PL can be explained by the four layered G that TEM suggests for PA (Figure 2g inset); it is worth mentioning here that single and bilayer G do not show PL and that PL decreases with increasing thickness of the flakes[30]. Therefore, G-AA and G-SA should have more layers compared to G-PA. This property of

disordered carbon films containing a mixture of sp^2 and sp^3 domains as a result of interaction is well reported, the sp^2 of GR gets clustered into sp^2 and sp^3 regions as a result of incorporation of foreign atoms[31].

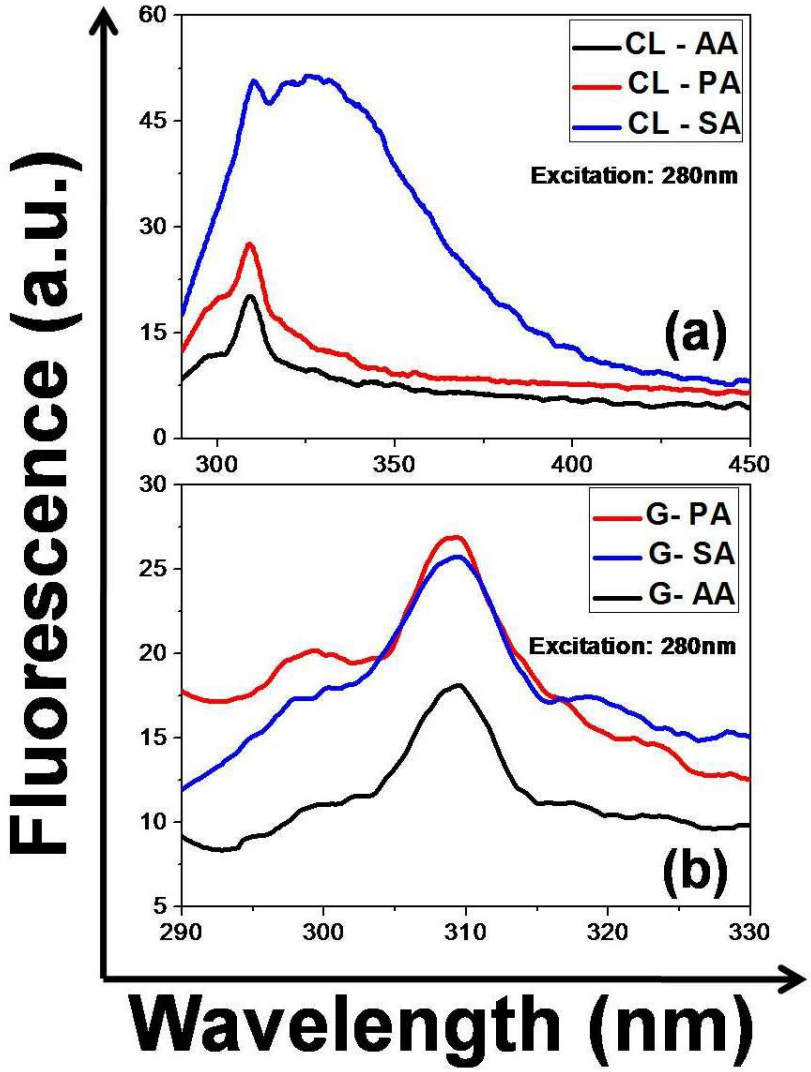

Figure 6. The FL spectra of (a) CL dispersion before and **(b)** after GR addition showing CL - GR interaction

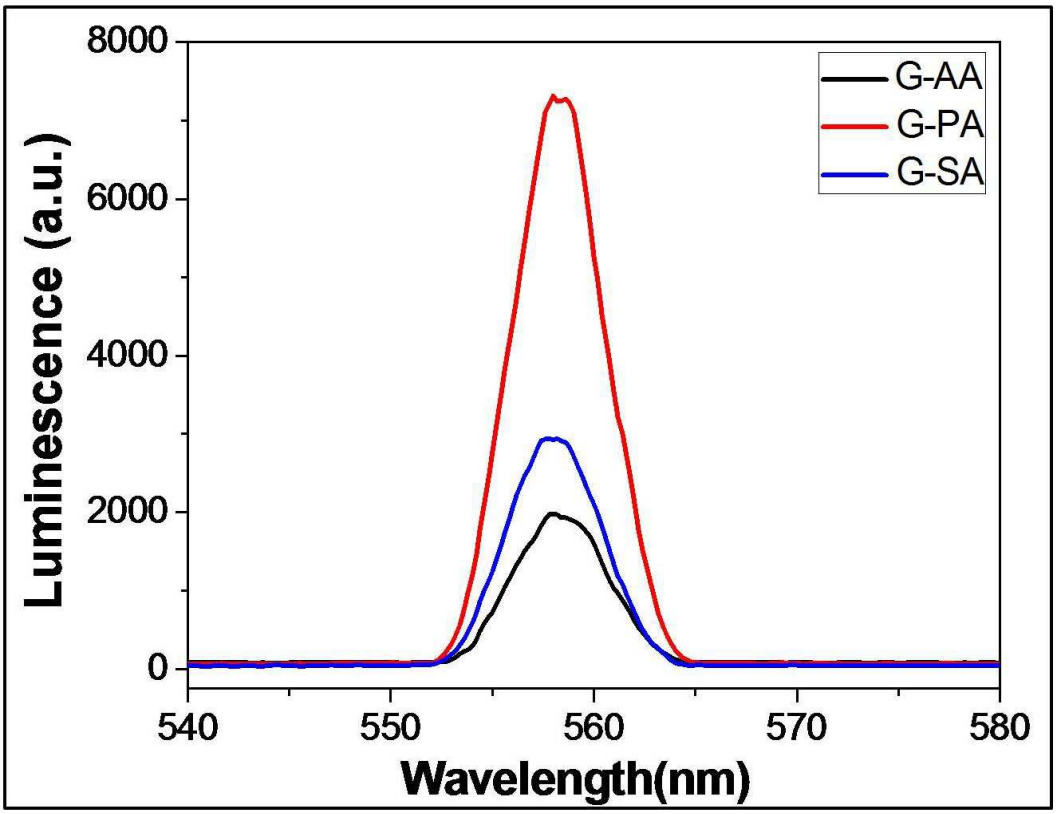

Figure7. The PL spectra showing CL-GR interaction

3.7 Cancer Studies. Nanoparticles are known to induce cytotoxicity through mitochondrial dysfunction and accumulation of intracellular ROS. Accumulation of intracellular ROS is indicative of oxidative stress; its level in cancer cells after incubation with G for 24 h was measured and dose-dependency observed. LDH release measures membrane damage, a hallmark of necrosis associated cell death, released into the extracellular medium as a result of membrane damage; consequently leading to apoptosis. Several studies have shown that nanomaterials can induce apoptosis or necrosis[32-34]. Our results (Figure 8) also suggested that the membrane integrity in cancer cells was compromised by G treatment in a dose dependent manner. G is known to induce cell death in cancer, its cytotoxic effects in cancer cell lines of three different origins (i.e. Solid cancer: FaDu, CAL-27, PC-3, DU-145 Hematological cancer: HL-60, K-562

and Neuronal Cancers: A172 and T98G) was evaluated. These cancer cell lines were incubated with various concentrations of G for 24 hours, and then the dose-dependent cytotoxicity was observed. In addition, our results firmly established that G has no cytotoxicity in HEK293, normal PBMCs, human keratinocytes and HUVEC cells confirming that G is not toxic to primary non cancerous cells. The large surface area of collagen modified G nanoplatelets possibly renders surface reactions potentially important, including ROS production and antioxidant depletion[35]. Our results are in agreement with previous reports establishing that G can trigger apoptosis through the activation of the mitochondrial pathway[32]. The induction of apoptosis and loss of viability was dependent on the size and concentration of G as well as the length of exposure[36-38]. G-PA was the best performing material among the three; this can be attributed to the specific inhibition of the over-expressed oncogenic signal transduction pathways (FAK, WNT, Notch, STAT1/3 and NRF-2 etc) originating at the cancer cell surface by the G-PA nanoflakes. However, clearly detailed mechanistic studies are required. Therefore, we are continuing with the mechanistic studies to delineate the specific effect of G-PA nanoflakes in each of the cancer cell types.

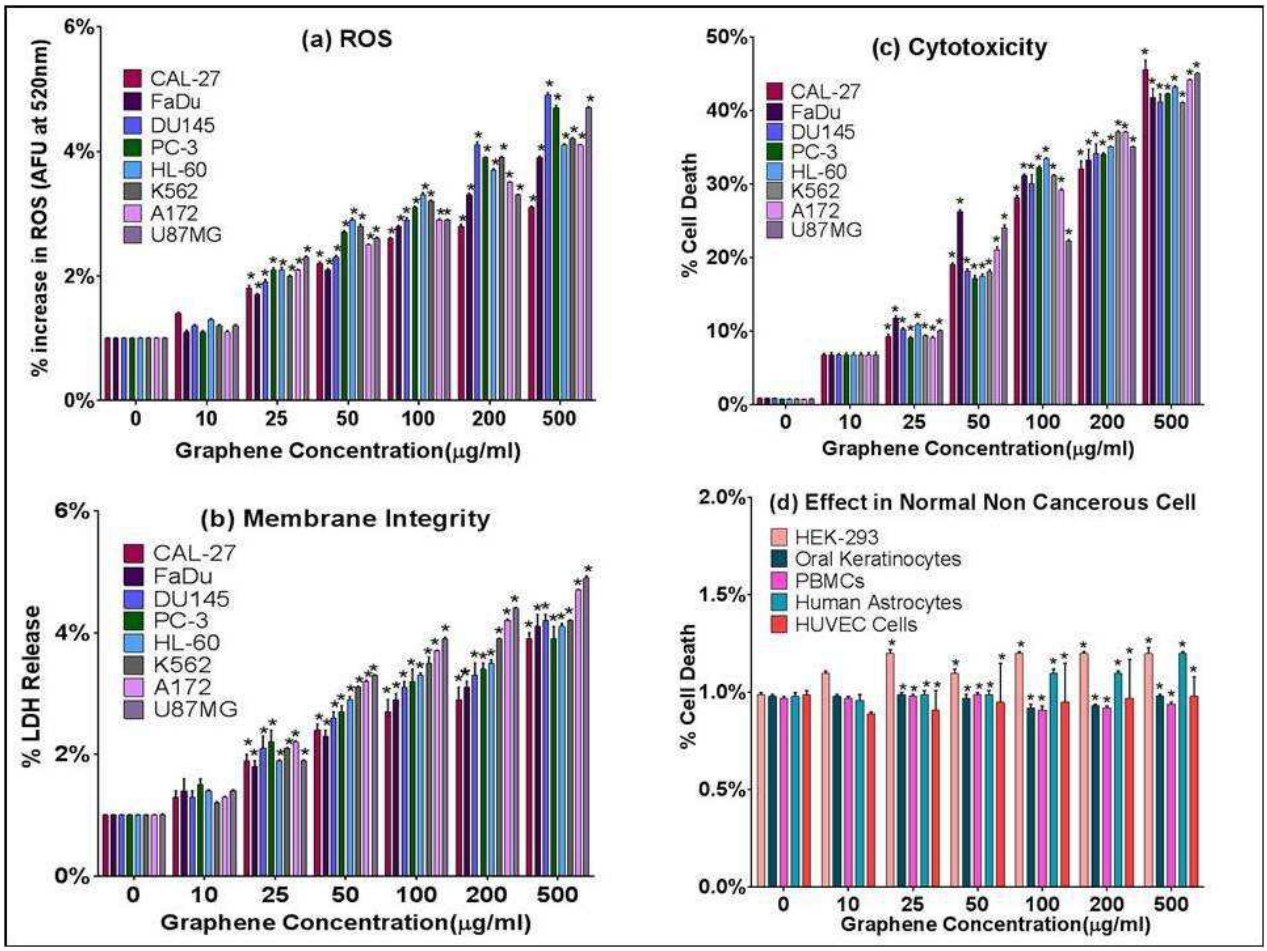

Figure8. Collagen modified G nanoplatelets induce ROS, affect membrane integrity and induce apoptosis in cancer cell. a) ROS, (b) the membrane integrity in terms of % LDH release, (c) the % cell death and (d) non-transformed cells of diverse origin were treated with same doses of G for 24 h. Data is expressed in means ± SD and represent the results of three independent experiments ($^{*}p < 0.05$)

4. CONCLUSIONS

We have studied the direct exfoliation of GR to collagen modified G using CL dispersed in three organic acids, biomimetically at ambient condition [39-40]. Acylated collagen has overcome many of the drawbacks of organic exfoliants namely, toxicity, cost and biocompatibility. The results

unambiguously prove that CL is capable of exfoliating GR in all three organic acids; PA being the best. The main challenge in G synthesis is to reduce aggregation by preventing re-stacking; CL dispersions in organic acids being proven surfactants increase the colloidal stability even at very mild sonication. The constant optical absorbance of conjugated systems at 660nm is also the least for G-PA showing that it is the least thick. G-PA with cancer cell lines of diverse origins indicates that it can be a promising nanomaterial with potential applications in nanotherapy of cancer. However, further validation in terms of its detailed mechanism of action is imperative to validate the findings reported in the present study.

NOTES

The authors declare no competing financial interest.

ACKNOWLEDGEMENT

S Bhattacharya would like to acknowledge the research support of CSIR-Senior Research Fellowship from the Government of India.

REFERENCES

[1] WS Hummers, RE Offeman, *J Am Chem Soc.,* 1958, **80**, 1339.

[2] S Park, RS Ruoff, *Nature .,* 2009,**4** , 217-24.

[3] Y Hernandez , V Nicolosi , M Lotya, FM Blighe, Z Sun, S De, IT McGovern, B Holland, M Byrne, YK Gun'Ko, JJ Boland, P Niraj, G Duesberg, S Krishnamurthy, R Goodhue , J Hutchison, V Scardaci, AC Ferrari, JN Coleman, *Nature Nanotech.,* 2008, **3** , 563-8.

[4] M Lotya, Y Hernandez, PJ King, RJ Smith, V Nicolosi, LS Karlsson, FM Blighe , S De , Z Wang , IT McGovern , GS Duesberg , JN Coleman , *J Am Chem Soc.,* 2009, **131(10)** , 3611-3620.

[5] X Wang, PF Fulvio, GA Baker, GM Veith, RR Unocic, SM Mahurin, M Chi , S Dai, *Chem Commun,* 2010, **46** , 4487- 4489.

[6] US patent, 4714758, 1987.

[7] W Du, X Jiang, L Zhu, *J. Mater. Chem. A*, 2013, **1**, 10592-606.

[8] MD Shoulders, RT Raines, *Annu Rev Biochem.,* 2009, **78**, 929-58.

[9] R Zacharia, H Ulbricht, T Hertel, *Phys Rev B.,* 2004,**69**, 155406-7.

[10] P Laaksonen, M Kainlauri, T Laaksonen, A Shchepetov, H Jiang, J Ahopelto, MB Linder, *Angew Chem Int Ed.,* 2010 ,**49(29)** ,4946-9.

[11] P Laaksonen, A Walther, JM Malho, M Kainlauri, O Ikkala, MB Linder, *Angew Chem Int Ed.,* 2011 ,**50**,8688-91.

[12] DNH Tran, S Kabiri, D Losic, *Carbon.,* 2014 ,**76**,193-202.

[13] P Dhar, S Bhattacharya, S Nayar, SK Das, *Langmuir*, 2015 **doi:** 10.1021/acs.langmuir.5b00067

[14] VK Srivastava, RK Gara, ML Bhatt, DP Sahu, DP Mishra, *Biochem Biophys Res Commun.,* 2011, **404**,40-5.

[15] N Rastogi, RK Gara, R Trivedi, A Singh, P Dixit, R Maurya, S Duggal, ML Bhatt, S Singh , DP Mishra, *Free Radic Biol Med.,* 2014 ,**68**,288-301.

[16] RDB Fraser, TP MacRae, A Miller, E Suzuki, *J Mol Biol.,* 1983 , **167**, 497-521.

[17] TJ Wess, A Hammersley, L Wess, A Miller, *J Mol Biol.,*1995, **248**, 487-93.

[18] TJ Wess, AP Hammersley, L Wess, A Miller, *J Mol Biol.,* 1998 , **275**, 255-67.

[19] R Kumar, R Sripriya, S Balaji, MS Kumar, PK Sehgal, *J Mol Struct.,*2011, **994**, 117-24.

[20] M Chaplin. Hydrophobic hydration. In: Water Structure and Science. http://www1.lsbu.ac.uk/water/ (accessed july 2014).

[21] M Quintana, J I Tapia, M Prato, *Belistein Journal of Nanotechnology.,* 2014,**5**,2328-2338.

[22] CSSR Kumar. Raman Spectroscopy for Nanomaterials Characterization. Springer-Verlag; Berlin: 2012.

[23] MA Pimenta, G Dresselhaus, MS Dresselhaus, LG Cancado, A Jorio, R Saito, *Phys Chem Chem Phys.,* 2007,**9**,1276-90.

[24] L Gong , RJ Young, IA Kinloch, SJ Haigh, JH Warner, JA Hinks, Z Xu , L Li , F Ding , I Riaz , R Jalil , KS Novoselov ,. *ACS Nano*., 2013, **7(8)**,7287-94.

[25] A Das, B Chakraborty, AK Sood, *Bull Mater Sci.,*2007, **31(3)**, 579-84.

[26] PK Chu, L Li, *Mater Chem Phys.,* 2006, **96**, 253–77.

[27] D Yang, A Velamakanni, G Bozoklu, S Park, M Stoller, RD Piner, S Stankovichc, I Junga,D A. Field, C A. Ventrice Jr, R S. Ruoff, *Carbon.,* 2009*,* **47(1)** *,* 145–52.

[28] JW Chiou, SC Ray, SI Peng, CH Chuang, BY Wang, HM Tsai, C W Pao, H J Lin, Y C Shao, Y F Wang, S C Chen, W F Pong, Y C Yeh, C W Chen, L C Chen, K H Chen, M H Tsai, A

Kumar, A Ganguly, P Papakonstantinou, H Yamane, N Kosugi, T Regier, L Liu, T K Sham, *J Phys Chem C.,* 2012, **116(30)** , 16251-8.

[29] J Robertson , *Phys Rev B.,* 1996 ,**53(24)** ,16302-5.

[30] S Kim, SW Hwang, M-K Kim, DY Shin, DH Shin, CO Kim, S B Yang , J H Park ,E Hwang , SH Choi , G Ko ,S Sim , C Sone , H J Choi , S Bae , B H Hong, *ACS Nano.,*2012, 6,8203–8.

[31] T Heitz, C Godet, JG Bouree, B Drevillon, J P Conde, *Phys Rev B.,*1999, **60**,6045-52.

[32] L Zhang, J Xia, Q Zhao, L Liu, Z Zhang, *Small.,*2010, **6**, 537–44.

[33] Y Chang, ST Yang, JH Liu, E Dong, Y Wang, A Cao, Y Liua, H Wang, *Toxicol.Lett,* 2011,**200**, 201–10.

[34] W Hu, C Peng, L Min, X Li, Y Zhang, N Chen, C Fan , Q Huang, *ACS Nano.,*2011,**5**, 3693–700.

[35] X Liu, V Gurel, D Morris, DW Murray, A Zhitkovich, AB Kane, R H Hurt, *Adv Mater.,*2007, **19**, 2790–6.

[36] O Akhavan, E Ghaderi, A , *Biomaterials., 2012 ,***33***, 8017–25.*

[37] C Cheng, S Nie, S Li, H Peng, H Yang, L Ma, S Sun, C Zhao, *J Mater Chem B.,* 2013, **1**,265–75.

[38] Y Wang, P Zhang, CF Liu, L Zhan, YF Li, CZ Huang, *RSC Adv.,*2012, **2,** 2322–8.

[39] S Bhattacharya, P Dhar, SK Das, R Ganguly, TJ Webster, S Nayar *Int J Nanomed.,* ,2014, **9** 1287–98.

[40] N Vitorino, JCC Abrantes, JR Frade, *App Energy.,* 2013, **104**, 890–7.

LEGENDS

Figure 1. A common schematic representation of GR exfoliation by acylated CL for all three acids

Figure2. TEM micrographs with indexed SAD patterns of (a-c) G-AA, (d-f) G-SA and (g-i) G-PA; the zone axis [z]=[0001] is mentioned for (c) and (i)

Figure3. AFM images showing the formation of collagen modified graphene nanoplatelets taken in the non contact mode; ΔZ signifies the difference in the height profile of (a) G-AA, (b) G-SA and (c) G-PA; (d) sectional analysis of the height along the length AB in the G-PA sample, the selected region is 550nm wide

Figure 4. Raman spectra showing the full spectra, G and 2D bands of (a-c) G-AA, (d-f) G-SA and (g-i) G-PA

Figure 5. XPS spectra of (a) GR, (b) G-AA, (c) G-SA and (d) G-PA dispersions. The increase in peak width and shift towards higher binding energy signify interaction of CL with GR

Figure 6. The FL spectra of (a) CL dispersion before and **(b)** after GR addition showing CL - GR interaction

Figure7. The PL spectra showing CL-GR interaction

Figure8. Collagen modified G nanoplatelets induce ROS, affect membrane integrity and induce apoptosis in cancer cell. a) ROS, (b) the membrane integrity in terms of % LDH release, (c) the % cell death and (d) non-transformed cells of diverse origin were treated with same doses of G

for 24 h. Data is expressed in means ± SD and represent the results of three independent experiments ($^{*}p < 0.05$)

TABLES

Table 1. Hydrodynamic diameter (D_H), zeta potential (**ξ)** and polydispersity index (PdI) of the G dispersions

Table2. Parameters showing binding energy (eV), chemical bonds, full width at half maximum (FWHM, eV), relative % concentration and sp^2/sp^3 ratio of spectral components of the deconvoluted C1s peaks